energies

MDPI

Article

A New Optimal Thermal-Based Adaptive Frequency Control for Bidirectional DC–DC Converter with Full-Range ZVS

Lulin Zhang [1], Shu Cheng [1], Jingtao Xu [2,*], Chaoqun Xiang [1] and Tianjian Yu [1]

[1] School of Traffic and Transportation Engineering, Central South University, Changsha 410017, China
[2] School of Automation, Central South University, Changsha 410017, China
* Correspondence: xjt4ugo@csu.edu.cn

Abstract: A new, optimal thermal-based adaptive frequency control (OTC) for a bidirectional DC–DC converter with full-range zero-voltage switching (ZVS) is presented in this paper. The proposed OTC achieves ZVS for a bidirectional DC–DC converter without any zero-crossing detection (ZCD) circuit or current sensor. In order to ensure a ZVS over a wide voltage and load range, the optimal switching frequency was adjusted by detecting and tracking the lowest junction temperature of the semiconductor device. Because the proposed OTC does not need a ZCD circuit, the complexity of the circuit and the susceptibility of the sampling noise are reduced. Additionally, compared with the expensive current sensor, the proposed method of temperature detection by the NTC thermistor decreases the cost. In addition, the proposed OTC does not need accurate circuit parameters and voltage or current sampling results, so the dependence on the parameters is reduced. Moreover, the temperature of the switch is directly monitored in the proposed OTC, which can effectively protect the device. A prototype with 16–32 V input and 48 V output was built, and the experiment results prove the effectiveness and feasibility of it.

Keywords: bidirectional DC–DC converter; adaptive frequency control; digital control; optimal temperature control; zero-voltage switching

check for updates

Citation: Zhang, L.; Cheng, S.; Xu, J.; Xiang, C.; Yu, T. A New Optimal Thermal-Based Adaptive Frequency Control for Bidirectional DC–DC Converter with Full-Range ZVS. *Energies* **2022**, *15*, 8250. https://doi.org/10.3390/en15218250

Academic Editor: Emilio Lorenzani

Received: 22 September 2022
Accepted: 2 November 2022
Published: 4 November 2022

Publisher's Note: MDPI stays neutral with regard to jurisdictional claims in published maps and institutional affiliations.

Copyright: © 2022 by the authors. Licensee MDPI, Basel, Switzerland. This article is an open access article distributed under the terms and conditions of the Creative Commons Attribution (CC BY) license (https://creativecommons.org/licenses/by/4.0/).

1. Introduction

With the great challenges of energy shortages and greenhouse effects, there has been a rapid growth in the demand of renewable energy and fuel-cell electric vehicles. In order to compensate the power mismatch in these applications, the bidirectional DC–DC converters are widely used between the energy storage device and the energy consumption device [1–3]. A bidirectional DC–DC converter which can store and dispatch electrical energy efficiently is the vital component for an energy storage system [4]. The typical directional DC–DC converter (synchronous boost converter) is shown in Figure 1.

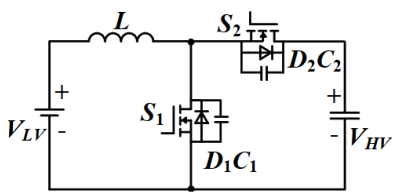

Figure 1. Topology of bidirectional converter.

In order to achieve high efficiency for the DC–DC converter, zero-voltage switching (ZVS) techniques are commonly used. In [5,6], an auxiliary resonant network was added and the ZVS of the MOSFETs was realized by the resonant current. However, the additional resonant network will increase the volume, and the parameter design of the resonant components is relatively complex. The additional auxiliary switches or clamp circuits were used in [7,8], but the circuit operation mode and control became more complex. In

addition to the improvement of the circuit structure, variable frequency modulation (VFM) is a simple and practical method. As for the bidirectional DC–DC converter, besides the continuous conduction mode (CCM), there also is a boundary conduction mode (BCM) which is achieved by VFM [9–11]. In the BCM, the direction of inductor current changes every cycle, which can realize the ZVS of all of the switches.

In order to make the converter work in the BCM under a wide voltage and load range, the switching frequency needs to be adjusted according to the working conditions. In [12–16], the external analog zero crossing detection circuit was used. The classical analog ZCD measures the current zero-crossing point by comparing the drain source voltage and the threshold voltage. However, the error of the voltage sampling and the inherent bias of the comparator will seriously affect the accuracy of the detection results. In order to improve the accuracy of the ZCD, some circuits which were developed with the voltage comparator compensation method were proposed to reduce the bias [17–19]. However, the additional circuits will increase the complexity of the circuit. The improved correction method was proposed to improve the detection accuracy and the efficiency of the ZCD [20–22]. However, it will cause switching delays in the semiconductor devices. In [23], a delay lock loop (DLL)-based ZCD was proposed for solving the delay problem by locking the pre-opening time of the comparator. Although some improved ZCD detection circuits can effectively improve the performance when they are compared to the traditional ZCD detection methods, the circuit structure becomes more complex, and the circuit cost increases.

In order to simplify the hardware circuit, a digital frequency control method with a simpler hardware structure is proposed. In [24,25], a digital adaptive frequency modulation with inductor current sensor was proposed and the switching frequency can be determined by a mathematical calculation based on the specific time inductor current sampling. It relies on inductor current sampling at a specific point. However, the value of the inductance changes with the current which will affect the calculation results. An alternative way to avoid the loading effects with the current measurements is the use of clamp-on current probes [26–28], but these generally have a limited accuracy [29] and require accurately selected values of the reversed current, the power inductor's inductance, and timing parameters to adjust the converter switching frequency and the dead times without using a duty ratio, which may cause the ZVS to become invalid. The method in [30] dynamically adjusts the switching frequency in a feed-forward manner sensed-inductor current to set the peak turn-off current, which can achieve a high efficiency in a wide operating range. However, it is not the best choice for its direct implementation on a controller platform since there are too many computations of the timing parameters. In [31], a simple analog control was presented to decrease the switching losses. However, it required an additional voltage conditioner and a high bandwidth and a highly linear current sensor. In a few words, these methods are highly dependent on the circuit parameters and the current sampling result, which will challenge the accuracy of the detection. To solve the problem, an empirical lookup table-based method that changed the switching frequency using the operating condition was proposed in [32]. For the applications with wide input and output voltages, there being a larger dimension of the table results in the storage capacity and computational complexity increasing. A complex calculation is somewhat difficult to implement. In addition, all of the methods in [24–32] require the high-precision and high-bandwidth current sensors. Thus, some researchers have studied current sensor-less control schemes [33,34], which can also reduce the sensitivity of the current sampling noise. Although expensive current sensors are not required, their calculation accuracy is low and they are not suitable for wide voltage and load applications.

In this paper, an optimal thermal-based adaptive frequency control (OTC) for a bidirectional DC–DC converter with full-range ZVS is proposed. The proposed solutions only need to detect the temperature of the semiconductor device and track the minimum temperature by adjusting the switching frequency. Since no additional zero-crossing detection circuit or current sensor is required, the proposed OTC is simpler, and its cost is lower. It should be noted, here, that the proposed OTC is not intended only for its implementation

in converters with light voltage-application variable switching frequency DCM operation. It can be used in high-voltage situations. Because the different voltage is related to the different optimal frequency. The OTC can also be used to adjust to the optimal frequency under different voltages. The detailed advantages are as follows:

1. The full-range ZVS can be achieved by the use of the proposed OTC, and there is no need for any expensive current sensors or complex ZCD circuits. Only the low-cost NTC resistors are required to detect the temperature which is much cheaper than the traditional methods are.
2. The proposed OTC to achieve full-range ZVS does not depend on accurate circuit parameters and voltage or current sampling values. Hence, the susceptibility of the parameters is reduced, and the control method is simple without the need for complicated calculations.
3. The temperature of the semiconductor device is directly monitored, which can effectively protect the device.

This paper is organized as follows. Section 2 discusses the power loss effects on the temperature and the analyses of the thermal simulation using the proposed algorithm. The proposed digital adaptive frequency modulation of the OTC with a full-range ZVS is described in Section 3. In Section 4, the implementation of the bidirectional DC–DC converter prototype with the proposed algorithm is described, and the proposed algorithm is verified with the experimental results, whereas the conclusion is given in Section 5. To achieve the experimental verification, a bidirectional boost converter with 16–32 V input voltage and 48 V output voltage was implemented.

2. Theory of Operation

2.1. Operation of Bidirectional Converter with BCM

The bidirectional circuit is extensively used in different kinds of energy storage system as a DC/DC foundation topology. Because S_1 and S_2 work in complementary conduction, the inductive current is always continuous. It can be divided into two cases according to whether the minimum current on the inductor has, respectively, a continuous conduction mode (CCM) with $I_{\min} > 0$ and $I_{\min} \leq 0$. The waveform of a bidirectional DC–DC converter is shown in Figure 2.

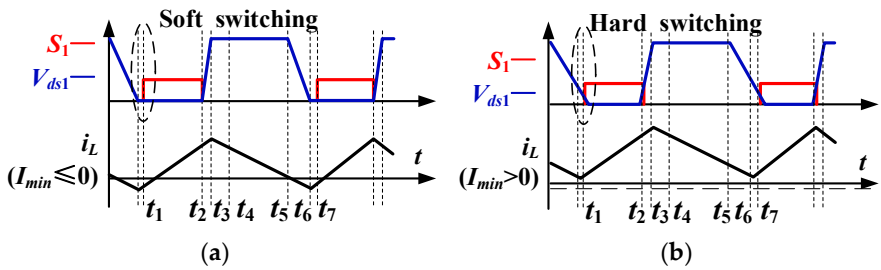

Figure 2. Waveforms of bidirectional converter with two conditions (**a**) $I_{\min} \leq 0$ (with ZVS) and (**b**) $I_{\min} > 0$ (without ZVS).

The output-side voltage V_{HV} and the input-side voltage V_{LV} are managed by the high-side switch S_1 and the low-side switch S_2, respectively. There is a dead time due to the charges or discharges of the inductor current between the on-times of the two switches. For example, from t_5 to t_7, the voltage across C_1 is reduced, while the voltage across C_2 rises. The drain–source voltage v_{ds1} is approximated linearly decreased to zero. After the drain–source voltage v_{ds1} drops to zero. The D_1 is turned on by clamping the drain–source voltage v_{ds1} at zero, which by creating the basis of S_1, turns on with the ZVS. As for a bidirectional DC–DC converter with the BCM, the inductor is chosen to perform the energy storage to achieve ZVS. During the dead time, the inductor current can be regarded as a constant current source to charge the capacitor C_2 and discharge C_1. The stored energy of inductor L is large enough for it to be relative to that of the capacitor. The inductor current

at t_6 is $I_{\min}$. The dead time needs to be longer than the charge time of C_2. To obtain the ZVS, the inductor current $I_{\min}$ at t_6 must be sufficiently negative, as follows:

$$I_{\min} < -\frac{2 \cdot C_2 \cdot V_{HV}}{T_{dead}} \tag{1}$$

The value of inductor L decide whether the inductor current direction can achieve the ZVS. Considering the extreme operate conditions, the inductor needs to be sized as following so that the current always crosses through zero.

As for the inductor, the induced voltage during the S_1 at this time can be expressed as:

$$V_{LV} = L\frac{di_L}{dt} = L\frac{2 \cdot P_{\max} \cdot f_{s_\min}}{D \cdot V_{LV}} \tag{2}$$

The minimum value of L should be satisfied:

$$L < \frac{(V_{HV} - V_{LV}) \cdot V_{LV}^2}{2 \cdot P_{\max} \cdot f_{s_\min} \cdot V_{HV}} \tag{3}$$

D is the duty ratio of S_1. $P_{\max}$ is the full-load power. $f_{s_\min}$ is the minimum frequency. V_{LV} is the low-side voltage, and V_{HV} is the high-side voltage. i_L is the inductor current.

Figure 3 shows the required inductance values of the BCM over the whole load range. The condition of V_{HV} = 48 V is plotted a as red line in Figure 3. For the different output voltage cases with a full load, the maximum allowable inductances are plotted in Figure 4. It can be seen that when the input voltage is low, the boost inductance values are at their lowest because the operating current is high. Therefore, the appropriate boost inductance value needs to be designed at a full load and at the lowest input voltage.

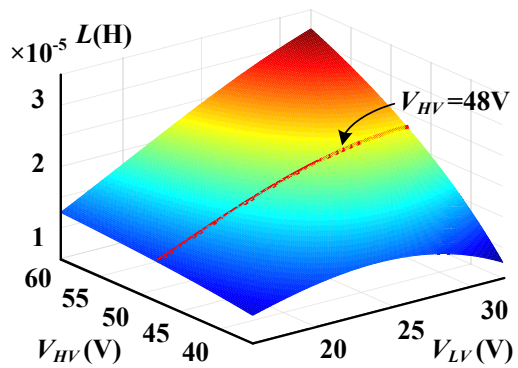

Figure 3. Critical inductance to operate in BCM with full load. The red line is the value of inductor V_{HV} = 48 V.

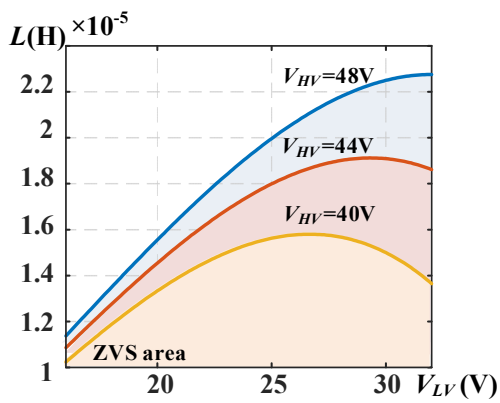

Figure 4. Critical inductance to operate in BCM with three different output voltage cases.

2.2. The Relationship between Switching Frequency and Switch Temperature

It can be deduced from the above analysis that there exists a high correlation between the switching frequency and the thermal factor. Thus, it is necessary to study the tradeoff between the switching frequency and the switching temperature. This part of the paper focuses on the corresponding temperature responses with the frequency of the semiconductor device in the bidirectional DC–DC converter using the OTC by introducing on an equivalent electro-thermal model of the power MOSFET.

The junction temperature of the MOSFET is customarily calculated using thermal resistance–capacitance (RC) networks that represent an equivalent of the heat transfer process from the chips to the heatsink, which can be described by the Fourier heat conduction equation:

$$q_x = -KA\frac{\partial T}{\partial x} \tag{4}$$

where K—thermal conductivity; A—heat conduction area of the materials; q_x—the heat produced or transmitted.

The Fourier heat conduction equation is a typical linear partial differential equation. The Cauer or Foster network can be used to model the heat conduction process. The Cauer network is more complex to use, which needs an scanning electron microscope (SEM) to analyze the material properties. However, the junction temperature is more important than the internal thermal distribution of the MOSFET chip is in this research. The Foster network was selected to fit the transient thermal resistance curve, as were four thermal resistance network layers of the model accuracy to achieve the rapid and accurate transient thermal resistance of the MOSFET.

$$Z_{th}(t) = \sum_{i=1}^{4} R_{thi}(1 - e^{-\frac{t}{R_{thi}C_{thi}}}) \tag{5}$$

The parameters of the Foster RC thermal model can be derived from a cooling curve and a curve fitting technique. The junction temperature of MOSFET can be expressed as:

$$T_j = P_{loss} \times (Z_{jc} + Z_{ch} + Z_{ha}) + T_a \tag{6}$$

where P_{loss}—the total loss power. The detailed derivation of the total loss is given in the Appendix A. Z_{jc}—the thermal impedance of the junction to the case. Z_{ch}—the thermal impedance between the case and the heat sink. Z_{ha}—the thermal impedance of the heat sink to the ambient environment.

An extra negative current $I_{\min}$ requires a higher $I_{\max}$ to produce the same average current which will increase the conduction losses. Thus, the switching frequency must be properly chosen to obtain an ZVS with a minimum $I_{\min}$. Figure 5 shows the junction temperature of the power device under a range of switching frequencies which were swapped at various loads. The dynamic nature of generating different power values and voltages according to the load conditions is the challenging factor in the field of DC/DC converters. The MOSFET in the boost circuit can operate at different switching frequencies, but only at certain switching frequencies can the MOSFET remain at the lowest operating junction temperature. The junction temperature versus switching frequency curves obtained from three fixed load condition is shown in Figure 6. For each load condition, the optimal switching frequency is not same.

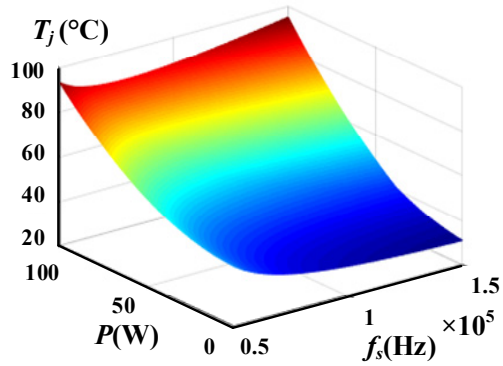

Figure 5. Operating junction temperature of power device.

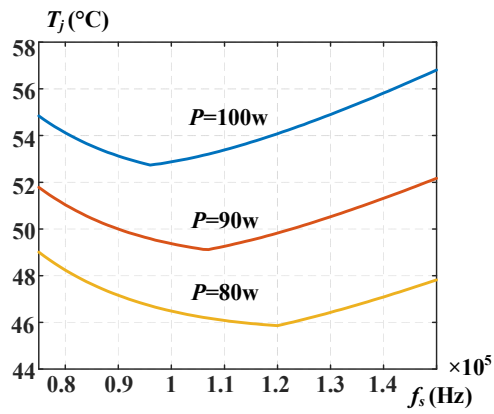

Figure 6. T_j–f_s curve with different load power.

3. Optimal Thermal-Based Adaptive Frequency Control

3.1. Optimal Temperature Control (OTC) Algorithm

The OTC for a bidirectional DC–DC converter with BCM can achieve a minimum junction temperature using the MOSFET by tracking the temperature of the power device under various conditions. In order to get the driver signal from the OTC, the turn-on and turn-off time of the MOSFET are figured out by a digital processor using the proposed algorithm. The switching frequency will be updated at a certain intervals based on the temperature feedback. This method operates without a current sensor or auxiliary ZCD circuits and instead, by directly measuring the junction temperature.

In this paper, the perturb and observe technique is used in the OTC algorithm since its offers simplicity and effectiveness. This algorithm perturbs the switching frequency to ensure that there is an optimal temperature. To make the MOSFET operate near the minimum temperature, the controlling methodology first detects the temperature using a temperature sensor. At an operating point on the T_j–f_s curve, if the switching frequency is adjusted in a given direction and $\Delta T_j < 0$, it is known that the perturbation will move the MOSFET's operating point toward the optimal temperature point. ΔT_j is the temperature difference of the previous step and the new step. Δf_s is the switching frequency difference of the previous step and the new step. Operating on the left of the optimal temperature point, it is obvious that incrementing (or decrementing) the switching frequency allows one to decrease (or increase) the temperature and increase (or decrease) the temperature when it is on the other side, while if the $\Delta T_j = 0$, the switching frequency remains at the previous step. The detailed steps are as follows, as shown in Figure 7.

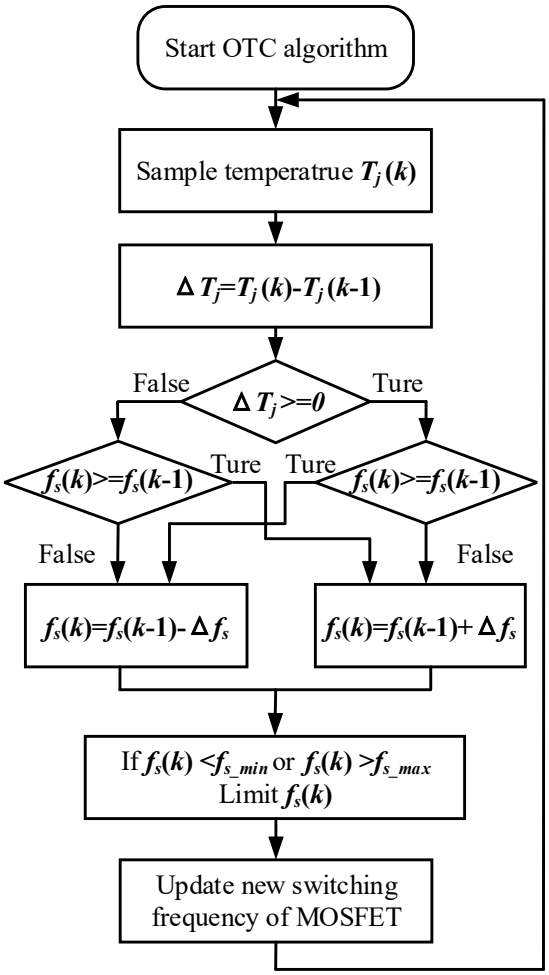

Figure 7. Flowchart of the proposed control algorithm.

Step 1: The temperature of the power device at the present time $T_j(k)$ is detected.

Step 2: Compare the temperature $T_j(k)$ with the previous moment and calculate the difference between them, which is defined as ΔT_j.

Step 3: Then, enter the part of judgement. The ΔT_j is checked to determine if it is positive or negative.

Step 4: In addition, it is necessary to judge the variable in the frequency.

Step 5: If ΔT_j is positive and the $f_s(k) \geq f_s(k-1)$, then the frequency at $k+1$ time should be reduced; if ΔT_j is positive, but the $f_s(k) \geq f_s(k-1)$ is not satisfied, then the frequency at k+1 time should be increased; if ΔT_j is negative and the $f_s(k) \geq f_s(k-1)$, then the frequency at k+1 time should be increased. On the contrary, if ΔT_j is negative and the $f_s(k) \geq f_s(k-1)$ is not satisfied, then the frequency at $k+1$ time should be reduced.

Step 6: Once the switching period is calculated, the $f_s(k)$ must be checked to determine if it is in the available frequency range.

Step 7: The new switching frequency of MOSFET should be updated.

3.2. Simulation of Proposed Method

To verify the above analysis, the proposed controller design was initially implemented in PLECS. The power device under the test junction temperature is S_1 because S_2 always works with ZVS. The simulation parameters were the same as they are in the experimental design, which are listed in Table 1.

Table 1. Parameters of the experimental prototype and simulation.

Designed Parameters	Value
Input voltage (V_{LV})	16–32 V
Output voltage (V_{HV})	48 V
Rated power (P)	100 W
Inductance (L_1)	10 µH
Core type	Kool Mµ
Capacitance (C)	100 µF
PI controller	K_p = 0.28, K_i = 2
MOSFET	IPP200N15N3G
Switching frequency	75–150 kHz

Figure 8 depicts a control block diagram of the proposed structure. The output voltage needed to be sampled. Then, the error value which next became a proportional integral was obtained by subtracting the output voltage from the reference voltage. The output of PI is the duty ratio D. On the other hand, the junction temperature had to be sampled and sent to the controller using the OTC. Thus, the optimal frequency based on the thermal factor can be calculated. Lastly, according to the duty ratio and optimal switching frequency, the driving signals of S_1 and S_2 were generated.

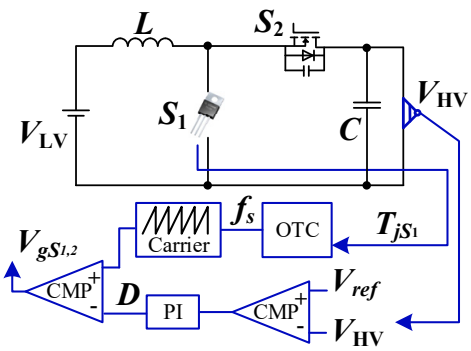

Figure 8. The proposed control block diagram.

Figures 9 and 10 show a comparison between the junction temperature ameliorations caused by the fixed switching frequency versus the proposed OTC algorithm, respectively; as it can be shown in the waveform, the OTC algorithm obtains a significant temperature reduction when it is compared with the fixed frequency method. From the full-load to half-load conditions, in Figure 9, the red line is operating without the OTC, and the blue line is operating with the OTC. As the curves show, a lower junction temperature was needed for it to operate with the OTC at the load condition change. On the other hand, Figure 9 shows that the junction temperature variation with the OTC is less than it is without the OTC between the half-load condition and the full-load condition. Figure 11 at V_{LV} = 24 V, at full load, the optimum switching frequency was at 138 kHz with the OTC. Compared to the temperature that was achieved without the OTC, it was significantly reduced by the OTC. The simulation results show that the OTC achieves the lowest temperature according to the direct feedback of the temperature at different loads.

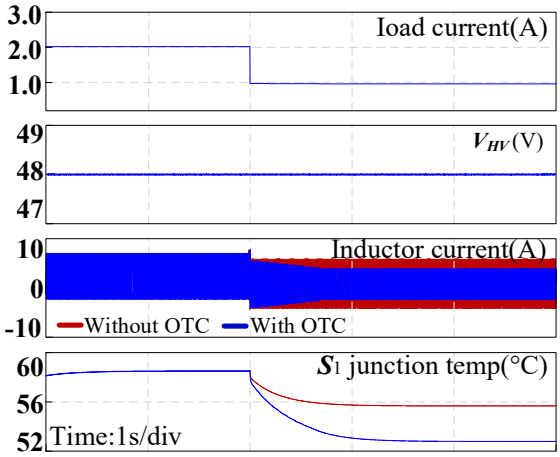

Figure 9. Simulation waveforms of 24 V input voltage to 48 V output voltage for a load current step from 2 A to 1 A with 100 W rated power.

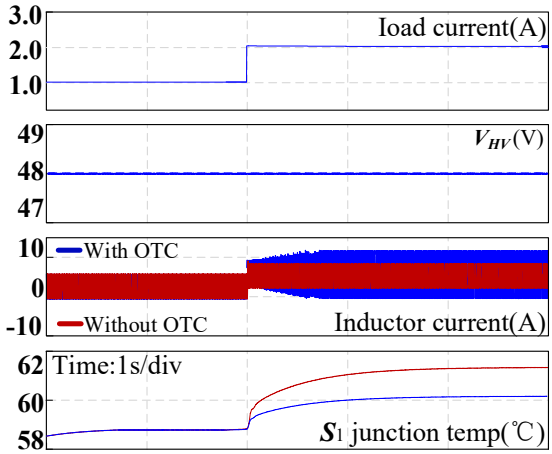

Figure 10. Simulation waveforms of 24 V input voltage to 48 V output voltage for a load current step from 1 A to 2 A with 100 W rated power.

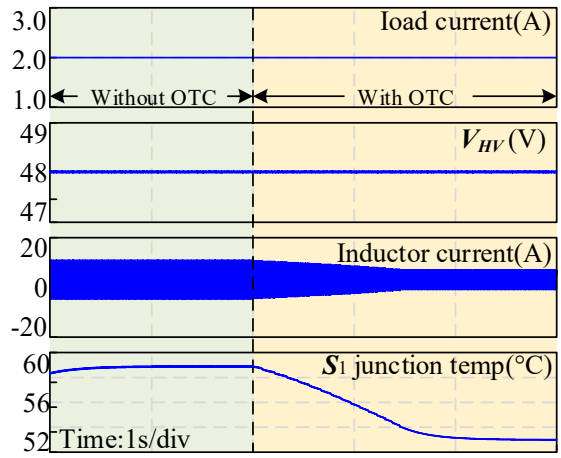

Figure 11. Simulation waveforms of the case that is being studied (24 V input voltage to 48 V output voltage with full load 100 W for fixed switching frequency convert to adaptive switching frequency).

3.3. Conparison of ZVS Methods

A comparison of the different ZVS topologies and BCM control methods proposed for the DC–DC converter are shown in Tables 2 and 3, respectively. The comparison of the topologies are made in terms of the number of switches, the passive components,

soft switching, switching frequency, efficiency, and output range. It can be seen that the proposed variable switching frequency modulation can achieve a high efficiency without any auxiliary device being used. In Table 3, the four aspects of cost, complexity, accuracy, and response speed are compared. The accuracy of the ZCD circuit is higher than those of the others, while the cost is the same among them. The sensor-less method cost low, but it has a complex circuit. The digital control one and the proposed OTC seem to have more advantages. It can be seen that the proposed OTC has a simple structure and a low cost. However, it should be noted that the ZVS will be temporarily lost when the working state changes rapidly. The proposed OTC is suitable for cases such as a battery energy storage system, for which its operation is relatively stable.

Table 2. The comparison with previous works.

Topologies	Traditional Boost Converter [35]	Active Clamping Boost Converter [36]	Quasi Resonant Boost Converter [37]	Bidirectional Converter in This Paper
Number of switches	1 MOSFET 1 Diode	2 MOSFET 1 Diode	1 MOSFET 1 Diode	2 MOSFET 0 Diode
Passive component	3	3	4	2
Soft switching	CCM/DCM	CCM/DCM	CCM/DCM	BCM
Switching frequency	Fixed frequency	Fixed frequency	Fixed frequency	Variable frequency
Efficiency	Low	High	High	High
Output range	Wide	Medium	Medium	Wide

Table 3. The comparison of BCM controls.

Method	ZCD [12–16]	Digital Control [24–32]	Sensorless [33,34]	Proposed OTC
Cost	High	Medium	Low	Low
Complexity	High	Medium	High	Low
Accuracy	High	Low	Low	Medium
Response speed	High	Medium	Medium	Low

4. Experiment

The performance of the proposed method was tested and evaluated on a 100 W bidirectional boost converter, as shown in Figure 12 with the parameters that are listed in Table 1. The digital microcontroller DSP was implemented to achieve both the proposed OTC method and the output voltage PI control.

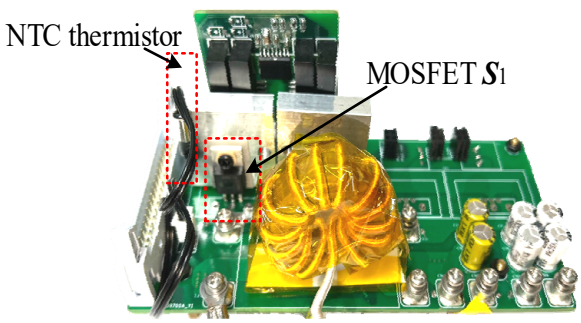

Figure 12. Experimental prototype of a bidirectional boost converter.

The indicator of the OTC is the temperature of the heat sink which was sensed by an NTC thermistor. To track the optimum temperature, the NTC thermistor feeds its measurement to the digital controller. Then, a new value of switching frequency is calculated.

The steady-state operation waveforms with a full load are shown in Figure 13. It can be seen that under different input voltages (16, 24, and 32 V), the switching frequency was adjusted adaptively by the proposed OTC, and the minimum inductor current $I_{\min}$ was less than zero. In addition, the voltage V_{ds1} reached zero before the gate pulse V_{gs1} was applicable to S_1. Hence, S_1 and S_2 can both achieve the ZVS. In addition, according to the ZVS analysis, the full load is the worst case for the ZVS. It can be concluded that the full operation range ZVS can be achieved with the proposed control algorithm.

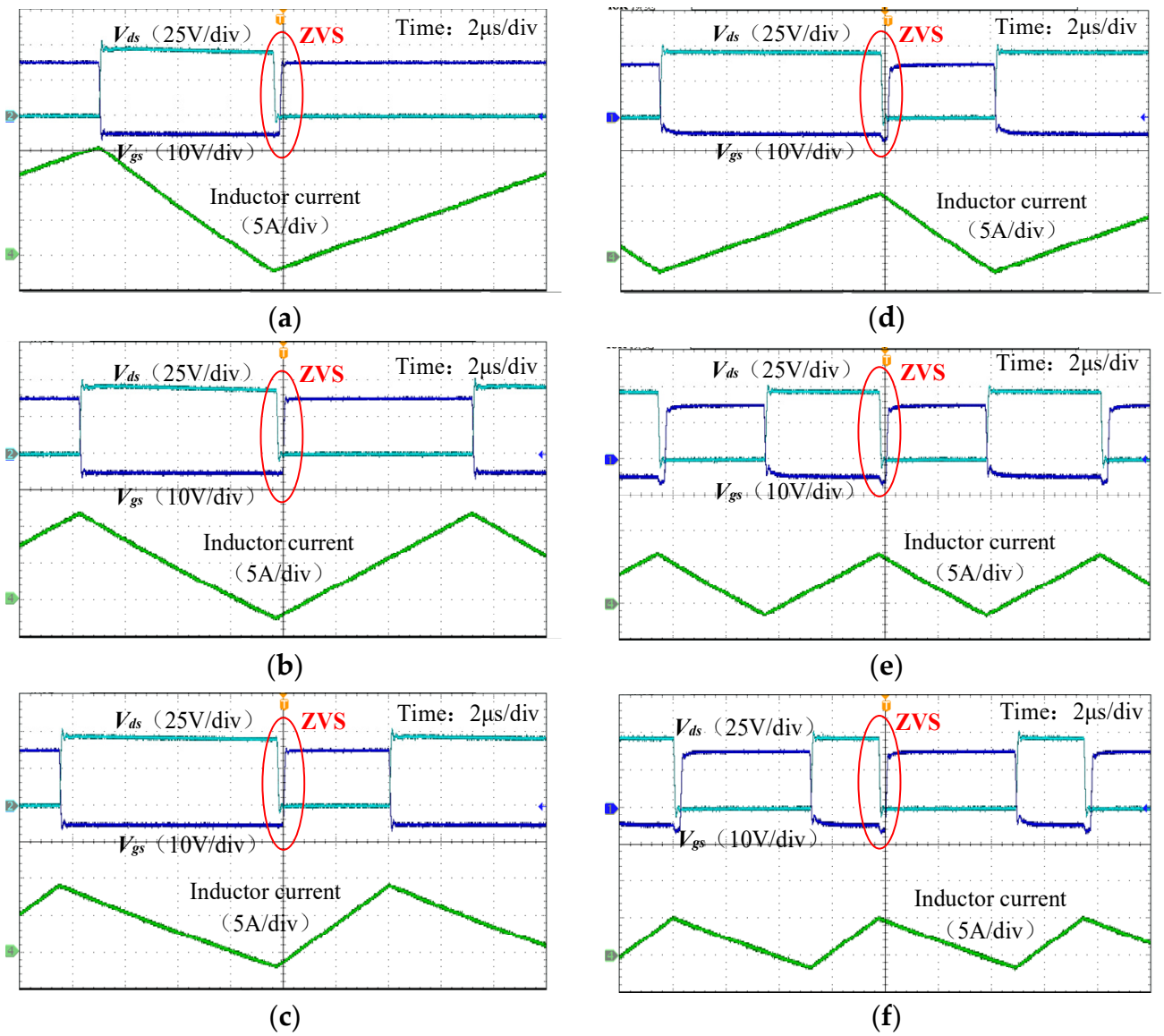

Figure 13. Experimental ZVS waveforms of the S_1. (**a**) V_{LV} = 16 V, full load; (**b**) V_{LV} = 24 V, full load; (**c**) V_{LV} = 32 V, full load. Experimental ZVS waveforms of the S_2. (**d**) V_{LV} = 16 V, half load; (**e**) V_{LV} = 24 V, half load; (**f**) V_{LV} = 32 V, half load.

The dynamic waveforms of the OTC are shown in Figures 14–16. The contrast waveforms of the proposed OTC are shown in Figures 14 and 15. It can be seen that the inductor current ripple was reduced with the proposed OTC method. Additionally, the $I_{\min}$ was kept at less than zero. The case of the temperature of S_1 with an optimal frequency is lower than the fixed frequency is, as shown in the thermal images. Figure 16 shows the dynamic response of the proposed OTC. In order to achieve a ZVS at a full load, the inductor current ripple is large, and the switching frequency is low. When the step to a half load state is taken, the switching frequency is increased, and the inductor current ripple is reduced by

the proposed OTC. In addition, Figure 17 shows that when the input voltage changed, the frequency changed depending on the temperature. In Figure 18, the efficiency curves of the OTC and traditional method according to the load are shown, which presents the high efficiency that was achieved in the proposed OTC. Thus, the optimal frequency for the temperature can be tracked with various voltages and load conditions.

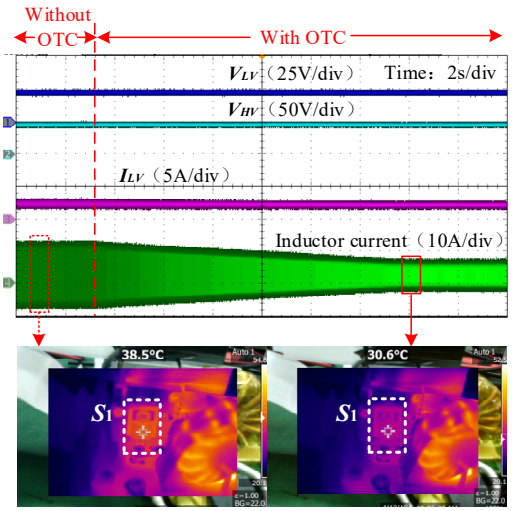

Figure 14. Experimental waveforms in V_{LV} = 24 V, half load.

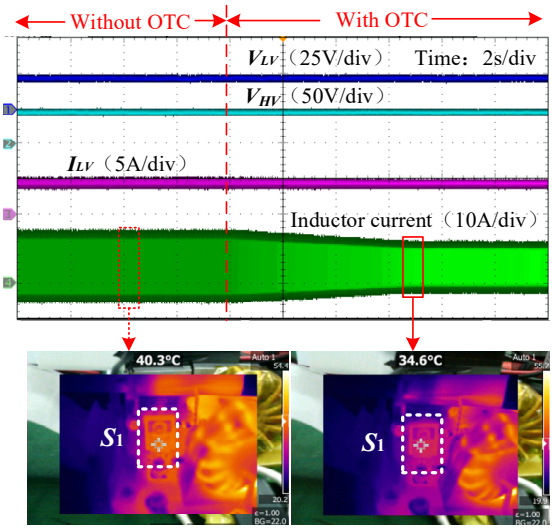

Figure 15. Experimental waveforms in V_{LV} = 24 V, full load.

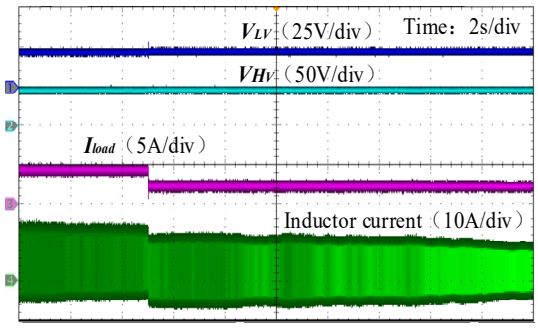

(**a**)

Figure 16. *Cont.*

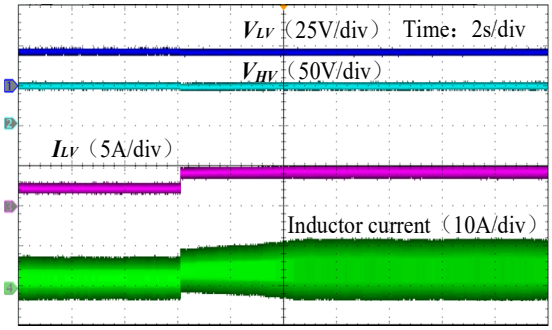

(**b**)

Figure 16. Experimental ZVS waveforms with (**a**) full-load step to half-load step in V_{LV} = 24 V; (**b**) half-load step to full-load step in V_{LV} = 24 V.

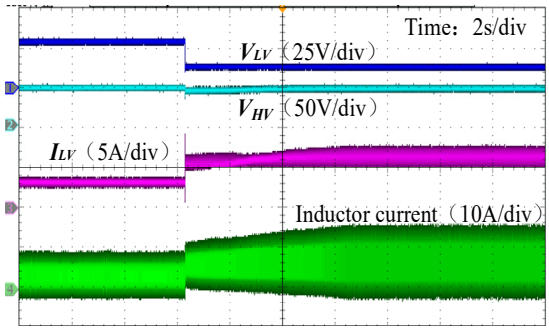

(**a**)

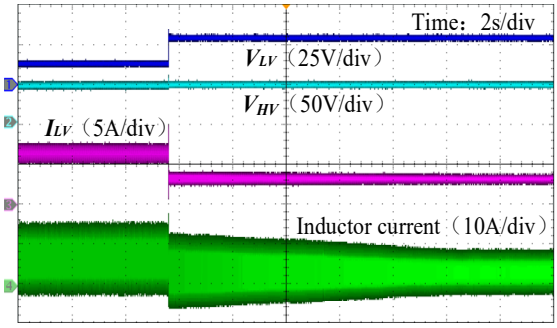

(**b**)

Figure 17. Experimental ZVS waveforms with (**a**) V_{LV} = 32 V step to 16 V step; (**b**) V_{LV} = 16 V step to 32 V step.

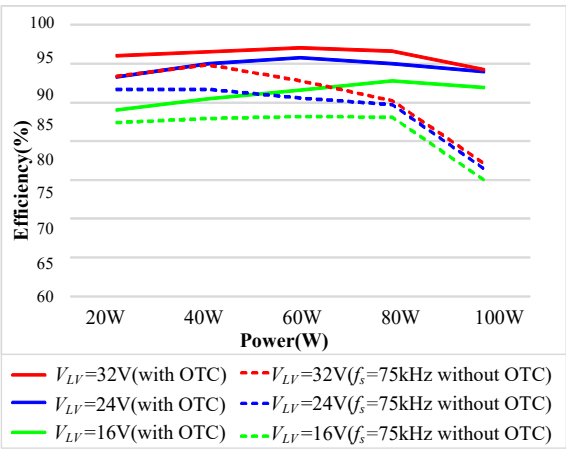

Figure 18. Experimental efficiency at different load comparison between OTC and traditional methods.

5. Conclusions

An optimal thermal-based adaptive frequency control (OTC) for bidirectional DC–DC converters has been proposed in this paper. This method directly adjusts the switching frequency by measuring the temperature. In addition, it can track the minimum temperature by adapting the optimal switching frequency which achieves a ZVS over a wide load variation. Additionally, the cost has been largely reduced by using the NTC thermistor without a ZCD or a current sensor. The effect on the thermal factor caused by switching the frequency and the feasibility of the optimal temperature digital controller under variable load conditions is analyzed in this paper. The proposed method is capable of significantly reducing the thermal of the power device and increasing the efficiency at any load value in the simulation and the experiment. It can protect the power module from failures resulting from having sustained operation temperatures. This new technology will be widely used in DC–DC converters to control the temperature effectively.

Author Contributions: Conceptualization, J.X.; data curation, C.X.; writing—original draft preparation, L.Z.; writing—review and editing, L.Z., J.X. and S.C.; funding acquisition, T.Y. and S.C. All authors have read and agreed to the published version of the manuscript.

Funding: This research was funded by the National Natural Science Foundation of China under Grant 52072414.

Data Availability Statement: Not applicable.

Conflicts of Interest: The authors declare no conflict of interest.

Appendix A

In the boost topology, MOSFET, as the main power device, will experience a considerable power losses. The MOSFET power losses mainly include conduction losses and switching losses. In forward power transmission, the device under analysis is S_1 since S_2 always turns on with zero voltages. S_1 with a ZVS and without a ZVS will cause the differences in switching losses, and the switching losses depend on the switching frequency. Conduction losses are a function of the load current, and they are junction temperature dependent. Thus, a mathematical, temperature-dependent MOSFET power losses model of two conditions is proposed in this part.

1. Loss analysis of $I_{\min} > 0$ (without ZVS)

   D is duty ratio of the S_1:

$$D = \frac{T_{on}}{T_{on} + T_{off}} \tag{A1}$$

   The ripple current of the input signal:

$$\Delta i_L = I_{\max} - I_{\min} \tag{A2}$$

   The average current of power device S_1 is:

$$I_a = \frac{1}{T}\int_0^{T_{on}} I_{S_1}(t)\, dt \tag{A3}$$

The integral part of the (A3) represents the area of the image that is enclosed by the input current I and the t-axis during the opening time.

When the current flowing through the MOSFET in the CCM mode is trapezoidal wave, as shown in the figure, the expression of current of S_1 is:

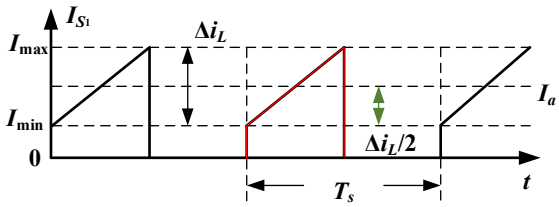

Figure A1. The current waveform of S_1 for $I_{\min} > 0$ (without ZVS).

$$I_{S_1} = \begin{cases} I_a - \frac{\Delta i_L}{2} + \frac{\Delta i_L}{T_{on}} \cdot t & (0 < t < T_{on}) \\ 0 & (T_{on} < t < T) \end{cases} \tag{A4}$$

According to the definition of root-mean-square:

$$I_{rms} = \sqrt{\frac{1}{T}\int_0^{T_{on}} I_{S_1}(t) \cdot dt} = \sqrt{\frac{1}{T}\int_0^{T_{on}} (I_a - \frac{\Delta i_L}{2} + \frac{\Delta i_L}{T_{on}} \cdot t) \cdot dt} = \sqrt{D \cdot (I_a^2 + \frac{\Delta {i_L}^2}{12})} \tag{A5}$$

The conduction loss of the MOSFET refers to the loss that is generated by the current in the switching resistance during the conduction time. Conduction power losses are a function of the RMS currents' squared values. The calculation formula of the conduction loss is as follows:

$$P_{con_CCM} = I_{rms}^2 R_{ds_on} = D(I_a^2 + \frac{\Delta {i_L}^2}{12}) \cdot R_{ds_on} \tag{A6}$$

$$R_{ds_on} = R_{ds_on25}(1 + K_{ds}(T_j - 25)) \tag{A7}$$

In the power loss estimation, the MOSFET on-state resistance R_{ds_on} is the main parameter that is temperature dependent. R_{ds_on25} is the on-resistance at junction temperature of 25, which can be obtained from datasheet. We used an on-resistance vs. junction temperature curve to get an approximate ratio K_{ds}.

Unlike the conduction loss, there is little temperature influence on the switching loss. The MOSFET switching losses include the turn on loss and the turn off loss. When the MOSFET is turned on, the drain–source voltage gradually decreases, and the drain current gradually increases. In this process, the overlapping parts are generated, which are the switching losses of the MOSFET. The switching power losses are a function of the switching frequency of the switches, the voltage across the switches, and current through the switches.

The drain–source voltage is:

$$v_{ds}(t) = V_{HV} - \frac{V_{HV}}{t_r} \cdot t \tag{A8}$$

The drain current is:

$$i_{ds}(t) = \frac{I_{\min}}{t_r} \cdot t \tag{A9}$$

The turn on loss is:

$$P_{on} = f_s \int_0^{t_r} i_{ds}(t) v_{ds}(t) dt = \frac{1}{6} V_{HV} \cdot (I_a - \frac{\Delta {i_L}^2}{2}) \cdot t_r \cdot f_s \tag{A10}$$

The turn off loss, as shown in the figure above, refers to the loss that is caused by the overlap of drain–source voltage rise and the drain current drop during the MOSFET turn off.

The drain–source voltage can be expressed as:

$$v_{ds}(t) = \frac{V_{HV}}{t_f} \cdot t \tag{A11}$$

The drain current is determined as:

$$i_{ds}(t) = I_{\max} - \frac{I_{\max}}{t_f} \cdot t \tag{A12}$$

Hence, the turn off loss can be calculated as:

$$P_{off} = f_s \int_0^{t_f} i_{ds}(t) v_{ds}(t) dt = \frac{1}{6} V_{HV} \cdot (I_a + \frac{\Delta i_L}{2}) \cdot t_f \cdot f_s \tag{A13}$$

The reverse-recovery loss P_{Qrr} is as:

$$P_{Qrr} = Q_{rr} \cdot V_{LV} \cdot f_s \tag{A14}$$

Q_{rr} is the reverse recovery charge.
The total loss of the MOSFET in the $I_{\min} > 0$ condition is:

$$P_{loss} = P_{con} + P_{on} + P_{off} + P_{Qrr} \tag{A15}$$

2. Loss analysis of $I_{\min} \leq 0$ (with ZVS)

When $I_{\min} \leq 0$, a ZVS operation mode is usually preferred, which allows a nearly lossless turn on, but as a consequence, there are losses during the turn off event. As long as the ZVS is reached, the current waveform on the inductor is different. The current flowing through the MOSFET is a triangular wave, as shown in Figure A2.

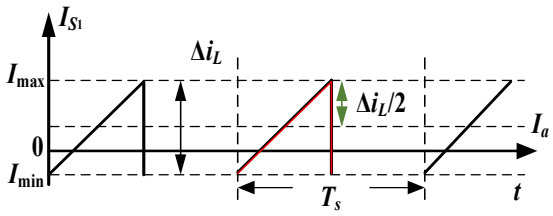

Figure A2. The current waveform of S_1 for $I_{\min} \leq 0$.

When $I_{\min} \leq 0$, the turn-on loss is:

$$P_{on} = f_s \int_0^{t_r} i_{ds}(t) v_{ds}(t) dt = \frac{1}{6} V_{HV} \cdot I_{\min} \cdot t_r \cdot f_s \leq 0 \tag{A16}$$

The conduction loss and the turn-off loss are the same as the first condition:

$$P_{con_CCM} = I_{rms}^2 R_{ds_on} = D(I_a^2 + \frac{{\Delta i_L}^2}{12}) \cdot R_{ds_on} \tag{A17}$$

$$P_{off} = \frac{1}{6} V_{HV} \cdot (I_a + \frac{\Delta i_L}{2}) \cdot t_f \cdot f_s \tag{A18}$$

The total loss of MOSFET in $I_{\min} \leq 0$ condition is:

$$P_{loss} = P_{con} + P_{off} + P_{Qrr} \tag{A19}$$

References

1. Xu, Q.; Vafamand, N.; Chen, L.; Dragičević, T.; Xie, L.; Blaabjerg, F. Review on Advanced Control Technologies for Bidirectional DC/DC Converters in DC Microgrids. *IEEE J. Emerg. Sel. Top. Power Electron.* **2021**, *9*, 1205–1221. [CrossRef]
2. Jiang, W.; Fahimi, B. Active Current Sharing and Source Management in Fuel Cell–Battery Hybrid Power System. *IEEE Trans. Ind. Electron.* **2010**, *57*, 752–761. [CrossRef]
3. Zhang, C.; Xu, B.; Jasni, J.; Radzi, M.A.M.; Azis, N.; Zhang, Q. Model Control and Digital Implementation of the Three Phase Interleaved Parallel Bidirectional Buck–Boost Converter for New Energy Electric Vehicles. *Energies* **2022**, *15*, 7178. [CrossRef]

4. Wu, H.; Sun, K.; Chen, L.; Zhu, L.; Xing, Y. High Step-Up/Step-Down Soft-Switching Bidirectional DC–DC Converter with Coupled-Inductor and Voltage Matching Control for Energy Storage Systems. *IEEE Trans. Ind. Electron.* **2016**, *63*, 2892–2903. [CrossRef]
5. Shen, J.; Khaligh, A. A Supervisory Energy Management Control Strategy in a Battery/Ultracapacitor Hybrid Energy Storage System. *IEEE Trans. Transp. Electrif.* **2015**, *1*, 223–231. [CrossRef]
6. Kim, N.-G.; Han, B.; Jo, S.-W.; Kim, M. High-Voltage-Gain Soft-Switching Converter Employing Bidirectional Switch for Fuel-Cell Vehicles. *IEEE Trans. Veh. Technol.* **2021**, *70*, 8731–8743. [CrossRef]
7. Khan, M.A.; Ahmed, A.; Husain, I.; Sozer, Y.; Badawy, M. Performance Analysis of Bidirectional DC–DC Converters for Electric Vehicles. *IEEE Trans. Ind. Appl.* **2015**, *51*, 3442–3452. [CrossRef]
8. Das, P.; Laan, B.; Mousavi, S.A.; Moschopoulos, G. A Nonisolated Bidirectional ZVS-PWM Active Clamped DC–DC Converter. *IEEE Trans. Power Electron.* **2009**, *24*, 553–558. [CrossRef]
9. Hwang, T.; Park, S. Seamless Boost Converter Control Under the Critical Boundary Condition for a Fuel Cell Power Conditioning System. *IEEE Trans. Power Electron.* **2012**, *27*, 3616–3626. [CrossRef]
10. Wu, H.; Lu, J.; Shi, W.; Xing, Y. Nonisolated Bidirectional DC–DC Converters with Negative-Coupled Inductor. *IEEE Trans. Power Electron.* **2012**, *27*, 2231–2235. [CrossRef]
11. Chiang, C.; Chen, C. Zero-Voltage-Switching Control for a PWM Buck Converter Under DCM/CCM Boundary. *IEEE Trans. Power Electron.* **2009**, *24*, 2120–2126. [CrossRef]
12. Qahouq, J.A.A.; Abdel-Rahman, O.; Huang, L.; Batarseh, I. On Load Adaptive Control of Voltage Regulators for Power Managed Loads: Control Schemes to Improve Converter Efficiency and Performance. *IEEE Trans. Power Electron.* **2007**, *22*, 1806–1819. [CrossRef]
13. Lee, C.-S.; Oh, Y.-J.; Na, K.-Y.; Kim, Y.-S.; Kim, N.-S. Integrated BiCMOS Control Circuits for High-Performance DC–DC Boost Converter. *IEEE Trans. Power Electron.* **2013**, *28*, 2596–2603. [CrossRef]
14. Yan, W.; Li, W.; Liu, R. A Noise-Shaped Buck DC–DC Converter with Improved Light-Load Efficiency and Fast Transient Response. *IEEE Trans. Power Electron.* **2011**, *26*, 3908–3924. [CrossRef]
15. Panov, Y.; Jovanovic, M.M. Adaptive off-time control for variable frequency, soft-switched flyback converter at light loads. *IEEE Trans. Power Electron.* **2002**, *17*, 596–603. [CrossRef]
16. Huang, Q.; Huang, A.Q. Variable Frequency Average Current Mode Control for ZVS Symmetrical Dual-Buck H-Bridge All-GaN Inverter. *IEEE J. Emerg. Sel. Top. Power Electron.* **2020**, *8*, 4416–4427. [CrossRef]
17. Wang, K.; Zhu, H.; Wu, J.; Yang, X.; Wang, L. Adaptive Driving Scheme for ZVS and Minimizing Circulating Current in MHz CRM Converters. *IEEE Trans. Power Electron.* **2021**, *36*, 3633–3637. [CrossRef]
18. Ren, X.; Zhou, Y.; Guo, Z.; Wu, Y.; Zhang, Z.; Chen, Q. Simple Analog-Based Accurate Variable On-Time Control for Critical Conduction Mode Boost Power Factor Correction Converters. *IEEE J. Emerg. Sel. Top. Power Electron.* **2020**, *8*, 4025–4036. [CrossRef]
19. Liu, C.; Lee, H.; Liao, P.; Chen, Y.; Chung, M.; Chen, P. Dual-Source Energy-Harvesting Interface with Cycle-by-Cycle Source Tracking and Adaptive Peak-Inductor-Current Control. *IEEE J. Solid-State Circuits* **2018**, *53*, 2741–2750. [CrossRef]
20. Zhang, X.; Chen, P.-H.; Okuma, Y.; Ishida, K.; Ryu, Y.; Watanabe, K.; Sakurai, T.; Takamiya, M. A 0.6 V Input CCM/DCM Operating Digital Buck Converter in 40 nm CMOS. *IEEE J. Solid-State Circuits* **2014**, *49*, 2377–2386. [CrossRef]
21. Radić, A.; Straka, A.; Prodić, A. Synchronized Zero-Crossing-Based Self-Tuning Capacitor Time-Constant Estimator for Low-Power Digitally Controlled DC–DC Converters. *IEEE Trans. Power Electron.* **2014**, *29*, 5106–5110. [CrossRef]
22. Michal, V. Inductor Current Zero-Crossing Detector and CCM/DCM Boundary Detector for Integrated High-Current Switched-Mode DC–DC Converters. *IEEE Trans. Power Electron.* **2014**, *29*, 5384–5391. [CrossRef]
23. Kim, J.; Shim, M.; Jung, J.; Kim, H.; Kim, C. A DC–DC Boost Converter with Variation Tolerant MPPT Technique and Efficient ZCS Circuit for Thermoelectric Energy Harvesting Applications. In Proceedings of the 2014 19th Asia and South Pacific Design Automation Conference (ASP-DAC), Singapore, 20–23 January 2014; pp. 35–36.
24. Liu, Y.-C.; Syu, Y.-L.; Dung, N.A.; Chen, C.; Chen, K.-D.; Kim, K.A. High-Switching-Frequency TCM Digital Control for Bidirectional-Interleaved Buck Converters Without Phase Error for Battery Charging. *IEEE J. Emerg. Sel. Top. Power Electron.* **2020**, *8*, 2111–2123. [CrossRef]
25. Baek, J.; Choi, W.; Cho, B. Digital Adaptive Frequency Modulation for Bidirectional DC–DC Converter. *IEEE Trans. Ind. Electron.* **2013**, *60*, 5167–5176. [CrossRef]
26. Reverter, F.; Gasulla, M. Optimal inductor current in boost DC/DC converters regulating the input voltage applied to low-power photovoltaic modules. *IEEE Trans. Power Electron.* **2017**, *32*, 8. [CrossRef]
27. Wang, J.-M.; Wu, S.-T. A Synchronous Buck DC–DC Converter Using a Novel Dual-Mode Control Scheme to Improve Efficiency. *IEEE Trans. Power Electron.* **2017**, *32*, 9. [CrossRef]
28. Reverter, F.; Gasulla, M. Optimal inductor current in boost DC/DC converters operating in burst mode under light-load conditions. *IEEE Trans. Power Electron.* **2016**, *31*, 15–20. [CrossRef]
29. Konjedic, T.; Korošec, L.; Truntič, M.; Restrepo, C.; Rodič, M.; Milanovič, M. DCM-Based Zero-Voltage Switching Control of a Bidirectional DC–DC Converter with Variable Switching Frequency. *IEEE Trans. Power Electron.* **2016**, *31*, 3273–3288. [CrossRef]
30. Sankaranarayanan, V.; Gao, Y.; Erickson, R.W.; Maksimovic, D. Online Efficiency Optimization of a Closed-Loop Controlled SiC-Based Bidirectional Boost Converter. *IEEE Trans. Power Electron.* **2022**, *37*, 4008–4021. [CrossRef]

31. Vazquez, A.; Martin, K.; Arias, M.; Sebastian, J. Variable-Width Hysteretic Analog Control for QSW-ZVS and TCM Source/Sink Converters. *IEEE Trans. Power Electron.* **2020**, *35*, 3. [CrossRef]
32. Lazar, M.C.; Shreelakshmi, M.P. Efficient Bidirectional DC-DC Converter Using Digital Adaptive Frequency Modulation. In Proceedings of the 2021 IEEE International Power and Renewable Energy Conference (IPRECON), Kerala, India, 24–26 September 2021; pp. 1–6.
33. Wang, J.-M.; Wu, S.-T. Sensorless control scheme for synchronous buck converter. *IET Circuits Devices Syst.* **2016**, *10*, 181–191. [CrossRef]
34. Abu Qahouq, J.A. Control Scheme for Sensorless Operation and Detection of CCM and DCM Operation Modes in Synchronous Switching Power Converters. *IEEE Trans. Power Electron.* **2010**, *25*, 2489–2495. [CrossRef]
35. Waffler, S.; Kolar, J.W. A Novel Low-Loss Modulation Strategy for High-Power Bidirectional Buck Boost Converters. *IEEE Trans. Power Electron.* **2009**, *24*, 6. [CrossRef]
36. Park, C.; Choi, S. Quasi-Resonant Boost-Half-Bridge Converter with Reduced Turn-Off Switching Losses for 16 V Fuel Cell Application. *IEEE Trans. Power Electron.* **2013**, *28*, 11. [CrossRef]
37. Wu, T.-F.; Lai, Y.-S.; Hung, J.-C.; Chen, Y.-M. Boost Converter with Coupled Inductors and Buck–Boost Type of Active Clamp. *IEEE Trans. Ind. Electron.* **2008**, *55*, 1. [CrossRef]